



Ab initio materials design using conformational space annealing and its application to searching for direct band gap silicon crystals



In-Ho Lee^a, Young Jun Oh^b, Sunghyun Kim^b, Jooyoung Lee^{c,*}, K.J. Chang^{b,**}

^a Korea Research Institute of Standards and Science, Daejeon 34113, Republic of Korea

^b Department of Physics, Korea Advanced Institute of Science and Technology, Daejeon 34141, Republic of Korea

^c Center for In Silico Protein Science, School of Computational Science, Korea Institute for Advanced Study, Seoul 02455, Republic of Korea

ARTICLE INFO

Article history:

Received 12 November 2015

Received in revised form

18 January 2016

Accepted 12 February 2016

Available online 26 February 2016

Keywords:

Conformational space annealing

Global optimization

Inverse materials design

ABSTRACT

Lately, the so-called inverse method of materials design has drawn much attention, where specific material properties are initially assigned and target materials are subsequently searched for. Although this method has been successful for some problems, the success of designing complex crystal structures containing many atoms is often limited by the efficiency of the search method utilized. Here we combine the global optimization method of conformational space annealing (CSA) with first-principles quantum calculations and report a new scheme named AMADEUS (*Ab initio* MAterials DEsign Using cSa). We demonstrate the utility of AMADEUS through the discovery of direct band gap Si crystals. The newly-designed direct gap Si allotropes show excellent optical properties and the spectroscopic limited maximum efficiencies comparable to those of best-known non-silicon photovoltaic materials. Our scheme not only provides a new perspective for the inverse problem of materials design but also may serve as a new tool for the computational design of a wide range of materials.

© 2016 Elsevier B.V. All rights reserved.

1. Introduction

One of the challenging problems in materials science is to accurately describe/predict the physical properties of materials based on the quantum theory. For a given material, where the structural information is known such as the chemical composition, lattice parameters, and atomic positions, first-principles electronic structure calculations in the framework of the density functional theory (DFT) [1] have been successful in describing its physical properties. On the other hand, the inverse of this problem [2] (known as the materials design problem) is to design/discover target materials where specific material properties are first assigned.

With the recent advance of computational power, materials design/engineering is currently being revolutionized. Several inverse methods have been proposed and used for a wide range of applications in materials design and discovery [3–6]. Thus, it is now possible to design new functional materials, not yet explored, at the atomic level by implementing an efficient search method together with first-principles DFT calculations [7–20]. Applications

include band gap engineering [21]; search for pressure-induced metastable phases [22]; designing of new alloys [23–25], perovskite [26], superlattices [27], topological insulators [28], semiconductor–metal clathrates [29], metal hydrates for superconductivity [30,31], photovoltaic materials [32–37], conducting polymers [38], and superhard materials [39].

For successful applications to specific problems, the inverse method needs a very efficient scheme for global optimization, which enables us to explore the configuration space of a given system under various environments, such as strain, pressure, and temperature. The “trial-and-error” algorithm is widely used to solve the inverse problem of materials design. However, since this algorithm is simply repeated with varied attempts until one decides to stop, its applicability to hard optimization problems is limited. A simulated annealing method [40] is often used when the search space is complex [41] and has been successful in finding stable structures by relaxing randomly generated configurations within a feasible computational time [5]. Other algorithms which showed good performance for materials design include basin hopping [42], minima hopping [43], and metadynamics [44]. Various genetic algorithms [7–9,14,45,46] and population-based evolutionary methods have been also implemented and tested [2,7,9,14,17,24] along with notable particle swarm optimization methods [15,38,47–49], and all of these methods require a great deal of computational

* Corresponding author. Tel.: +82 29583731; fax: +82 29583890.

** Corresponding author. Tel.: +82 423502531; fax: +82 423502510.

E-mail addresses: jlee@kias.re.kr (J. Lee), kjchang@kaist.ac.kr (K.J. Chang).

power. Currently, the major bottleneck of the materials design based on first-principles electronic structure calculations appears to be the efficiency of the global optimization scheme utilized.

In this work, we propose a protocol named AMADEUS (*Ab initio* MAterials DEsign Using cSa) which is designed to search for new functional materials through computer simulations. In this protocol, the conformational space annealing (CSA) algorithm [50,51] for global optimization is combined with first-principles electronic structure calculations. The current work is motivated by a series of recent successful applications to many hard optimization problems, which showed the superiority of CSA over other existing global optimization methods [52–54]. We demonstrate the utility of AMADEUS for first-principles materials design by applying it to the design of direct band gap Si crystals. Some of the results were given elsewhere [55].

In the following, we describe the implementation of the CSA global optimization scheme along with first-principles electronic structure calculations in materials design. We provide the details of the CSA procedures during computer simulations. Then, we utilize our scheme to explore direct band gap Si crystals, as a case study, and discuss the structural and electronic properties of the designed allotropes, followed by conclusion.

2. Methods

The goal of the computational materials design is to discover materials with specific target properties. Many approaches have been proposed to solve the inverse problem of materials design [2,5,17,28,29,32,33,36,38,39]. These approaches have a common theme of efficient structure search, which generally relies on the combination of global optimization with materials characterization. While the search method varies with the pre-assigned physical property, we adopted first-principles calculations to characterize the material properties.

As shown in the Lennard-Jones cluster energy optimization problem, the number of local energy minima of a combinatorial optimization problem typically scales exponentially with the system size [51,56], thus making it intrinsically difficult to obtain robust answers by a search method for medium to large size problems. Therefore, in order to draw meaningful and comprehensive conclusion from a computational study of materials design, one should start with an energy function that provides an accurate energy landscape of the intended material and then explore the landscape by applying the best sampling strategy available. The CSA algorithm for global optimization has been successfully applied to various difficult combinatorial optimization problems, including protein structure prediction [57–60], the global optimization of Lennard-Jones molecular clusters [51], and the modularity optimization for network community detection [61]. Recently, the CSA algorithm has been successfully used to explore direct band gap Si crystals [55,62]. Here we provide detailed descriptions of our computational approach in conjunction with first-principles calculations for materials design.

2.1. Objective function

In the global optimization problem, the ultimate goal is to obtain the most optimal solution in terms of the given objective function, and this also applies to the case of CSA in a sense. However, the goal of CSA is more ambitious because it is desirable to obtain not only the most optimal solution but also many distinct sub-optimal solutions. In all cases where CSA was previously applied except for the case of materials design, the function to be minimized by using a local minimizer was identical to the objective function to be optimized. However, in AMADEUS, the local minimization was performed for the total energy or

enthalpy, and after the minimization was finished, the fitness of the minimized solution was evaluated by the objective function relevant for the target properties. Here we point out that the terminology of energy is interchangeably used to represent the enthalpy of a material under a certain pressure.

The objective function should be designed in such a way that the most optimal solution should correspond to the most desired solution in terms of the target property. Since the current version of AMADEUS only deals with systems with given compositions, we focus on crystal structures. For a system with n atoms per unit cell, the structure search is accompanied by optimizing the $6 + 3n$ degrees of freedom that include six lattice parameters (a, b, c, α, β , and γ) and the set of atomic positions ($\{R_i\}$). Here a, b , and c are the lattice constants in the unit cell and α, β , and γ are the angles between the lattice vectors.

For a given material design problem, the proper design of its objective function is one of the most important factors for success. Here we provide examples of the objective functions applicable to various designs. When searching for stable crystal phases at a given external pressure, one obvious choice for the objective function is the enthalpy. If an analytic expression for the function as well as the gradient of enthalpy [63,64] is available, the CSA algorithm can be applied to the objective function in a straightforward way.

For the optical and electrical properties of semiconductors, their electronic structure should be investigated. Often direct band gap materials are preferred for an efficient energy transfer between the optical and electrical energies. For this, one has to identify both direct and indirect band gap sizes in electronic structure. We will discuss this in more detail later.

Other quantities such as density of states, spin–orbit coupling, and Debye temperature, can be also considered as the objective function for a specialized materials design. For example, the ability of a given material to produce thermoelectric power is related to its dimensionless figure of merit, defined as

$$ZT = \frac{S^2 \sigma_e T}{\kappa}, \quad (1)$$

where S, σ_e, κ , and T denote Seebeck coefficient, electrical conductivity, thermal conductivity, and temperature, respectively [29,65]. The ideal band structure for a good thermoelectric-power material would have a large number of valleys closely packed around its band edges. Therefore, a large density of states near the band edge is a desirable quantity for good thermoelectric materials. When searching for novel superconductors [66], the Debye temperature and/or a large density of states at the Fermi level can be used for the objective function. In topological insulators, the protected surface states can be explained by a band inversion induced by the spin–orbit coupling at the \bar{k} -points with time reversal symmetry in the Brillouin zone [28]. Therefore, the strength of the spin–orbit coupling can be used as an objective function when searching for topological insulators.

2.2. Conformational space annealing for global optimization

In order to sample the conformational space of a given material with a target property, we used a variant of the CSA algorithm. That is, a variant of CSA was used to generate many distinct low-energy crystal structures with pre-assigned target electronic properties. The variation is in the plot that the local minimization was performed in the total energy/enthalpy, but the objective function of a thus-minimized solution was evaluated in terms of its target property. Although we focus on the band gap engineering of Si allotropes, the current method can be easily applied to optimize any other properties of a material.

The CSA algorithm provides a systematic way to generate numerous solutions which are diverse and yet optimal in their

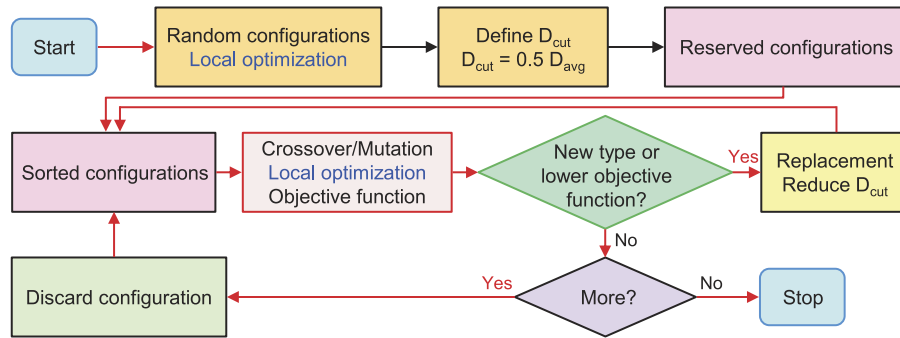


Fig. 1. Flowchart of the CSA approach for the inverse method of materials design. Red colored arrows stand for parallel computing processes. The initial distance measure D_{cut} is determined from the average of distances (D_{avg}) between starting configurations. (For interpretation of the references to color in this figure legend, the reader is referred to the web version of this article.)

objective function values. To apply CSA to a global optimization problem, three ingredients are needed: (i) a local energy/enthalpy minimizer, (ii) a way to generate a daughter solution from one or two parent solution(s), and (iii) a measure to estimate the difference or similarity between two given solutions. Since CSA follows multiple trajectories of local energy minima, it can be considered as a genetic algorithm in a broad sense [45]. In the genetic algorithm, a population of current solutions evolves toward the next generation of better solutions.

Fig. 1 shows the flowchart of CSA for the crystal structure sampling. The immediate goal of CSA is to generate many distinct solutions with low objective function values. In this process, special care is applied to control the diversity in the sampled solutions. Annealing is performed in an abstract solution space so that in the early stages of CSA, diversity of the solutions is kept rather high, and even in later stages diverse solutions with low objective function values are kept in the population. To control the sampling diversity, a special procedure is taken, which will be discussed in the following subsection. The key difference between the current variation of CSA and the usual CSA is that the local minimization is performed in terms of the energy or enthalpy, but the objective function of the minimized solution is measured by its electronic structure properties.

We consider the conformational space which consists of N_{bank} (typically 50, but an arbitrary number) conformations, which are generated in a random fashion. The energies of these conformations are all subsequently minimized by using a local minimizer, which is the first ingredient of CSA. For the energy minimization, first-principles calculations are performed, where the minimization variables are atomic positions and lattice parameters. We note that, when using a plane wave basis set for electronic structure calculations, a high energy cutoff value is required for accurate calculations of stress tensors [63,64].

In the following step, daughter conformations are generated by mutation (random perturbation of a single parent conformation) and crossover (combination of two parent conformations) procedures, which belong to the second ingredient of CSA [45]. We note that the appropriate ratio of mutation to crossover is 1:4 to keep the diversity of solutions. All daughter conformations are subsequently energy minimized by the local minimization procedure. The last and third ingredient of CSA, the difference or similarity measure between two given solutions, is used to prevent the coexistence of similar solutions in population.

2.3. Key CSA procedure

The key procedure of CSA is as follows. At each stage, N_{bank} solutions are chosen in the sampling population of CSA after their energies are locally minimized and their objective function

values are evaluated. Numerous daughter solutions are generated by the aforementioned mutation and crossover procedures, and they are all subject to the procedure of local energy minimization and subsequent objective function evaluation, which constitutes the most time-consuming part of CSA. Since this procedure can be performed in a separate and independent manner, the whole calculations can be efficiently executed in a highly parallel fashion even by using a slow node-to-node network communication protocol such as the ethernet connection [67].

Using each daughter solution σ , the population of the current CSA solutions is updated as follows. Out of N_{bank} current solutions, the closest one to σ is identified, which is called Σ . If the current annealing parameter D_{cut} is greater than the distance between σ and Σ (denoted as $D_{\sigma\Sigma}$), σ is considered to be similar to Σ , and σ can replace Σ if it is of better objective-function value than Σ (otherwise σ is discarded). But, if $D_{\sigma\Sigma} \geq D_{cut}$, σ can replace the solution ω with the worst objective function value in the population if σ is of better objective-function value than ω . It is easy to picture that the diversity of the sampled population can be controlled by D_{cut} . We set D_{cut} to a large value in the early stages of CSA, and then gradually reduced it to a smaller value (but never to zero). We point out that maintaining diversity is a necessary but not a sufficient condition for the good performance of CSA. Additionally, in order to cover the whole low-lying basin areas in the landscape of the objective function, new types of solutions must be continuously supplied by the mutation/crossover procedures as much as possible.

2.4. Implementation of highly parallel CSA

In the parallel version of the CSA algorithm, there are two kinds of jobs: (1) The master process takes care of all the CSA-related but less CPU intensive chores such as generating trial conformations by mutation and crossover procedures, distributing trial conformations to slave processes, collecting minimized trial conformations from slave processes, and updating the bank conformations with minimized trial conformations based on their objective function values, etc. (2) The slave processes execute highly CPU intensive jobs such as the local energy/enthalpy minimization of threaded trial conformations provided by the master process and the evaluation of the objective function values for minimized trial conformations. Therefore, time-consuming first-principles calculations are performed by the slave processes, and these calculations can be done efficiently by using multiple cores within a node (each node has 20 CPU cores in our system).

Our computations were performed in the “parallel-in-parallel” fashion as follows. In AMADEUS, the master and slave processes were operated separately, and their communication is executed via disk files. For convenience, AMADEUS creates 50 (an arbitrary

number) directories to be used repeatedly for first-principles calculations. Initially, the master process passes over 50 trial solutions to be minimized to the 50 directories, each of which queues a job for a slave process using a node containing 20 CPU cores. Whenever a slave process finishes its quantum calculations, it creates the following output files in its directory; the crystal structure of the minimized solution, the objective function value, and a job-status-indicating marker. The master process constantly monitors the job-status-indicating markers of all 50 directories. Whenever it finds that a job is finished in a directory, it retrieves the outputs, updates the current bank conformations using the retrieved outputs, generates a trial conformation, and queues another slave job by writing down necessary input files of the trial conformation in the just-finished directory. Since the time interval between finding a job finished and queuing a new job is much less than the time a slave process needs to finish its job, at a given time, there are always 49–50 jobs either running or in the queue.

Since hundreds of trial conformations can be easily prepared to be minimized at any moment in AMADEUS, theoretically, by using a larger number of directories than 50, we could have utilized thousands of CPU cores with almost perfect parallel efficiency. In practice, on average, we used about 25 nodes (500 CPU cores) at a time from our local multi-user-shared Linux machine.

2.5. Details of CSA procedures

In this section, we describe additional details of the CSA procedure in AMADEUS that were implemented for the inverse design of materials. Once the solution representation and the objective function are defined, the CSA algorithm starts by initializing its bank population of solutions. Then, the population is iteratively improved by (i) generating trial solutions by mutation and crossover, (ii) performing local minimization of generated trial solutions and subsequently evaluating their objective function values, and (iii) updating bank conformations by using minimized trial solutions with their objective function values.

2.5.1. Generation of initial crystal structures

An initial population of the CSA sampling was constructed by generating $N_{bank} = 50$ trial conformations in a random fashion followed by short Monte Carlo simulations to remove atomic core-to-core overlaps. To generate a trial conformation, first, the unit cell of the intended crystal was generated in a random fashion but with the restriction that its lattice parameters (a, b, c, α, β , and γ) satisfy the following conditions: $20^\circ \leq \alpha \leq 160^\circ$, $20^\circ \leq \beta \leq 160^\circ$, $20^\circ \leq \gamma \leq 160^\circ$, $a > 1.2 \text{ \AA}$, $b > 1.2 \text{ \AA}$, $c > 1.2 \text{ \AA}$, $0.3 \leq a/b \leq 6.0$, $0.3 \leq b/c \leq 6.0$, and $0.3 \leq c/a \leq 6.0$.

Then, the lattice constants (a, b , and c) were uniformly multiplied by a constant factor in a random fashion so that the cell volume fell between 88% and 112% of that of the reference structure. As the reference structure, we took one of the existing structures of the intended material, for example, the diamond structure in Si. Once the cell's shape and size were set as above, its constituting atoms were initially positioned in a random fashion within the cell, which typically contained atomic core-to-core clashes causing anomalous divergence in quantum calculations. Therefore, prior to launching first-principles calculations, unfavorable ionic positions causing core-to-core overlaps were adjusted [68] by performing short Monte Carlo simulations, where the maximum size of positional perturbation was set to one half of the Wigner–Seitz radius. Typically, 100 Monte Carlo steps were sufficient to remove all overlaps.

2.5.2. Selection of parent solution(s)

In order to generate trial solutions, one (for mutation) or two (for crossover) solutions in the current bank conformations need to be selected, the details of which will be given in the following subsections. First, the current bank conformations are ranked according to their objective function values from 1st to N_{bank}^{th} . Using the conformation's rank, we generated an exponential distribution [69] for the selection probability as follows. For a random number r uniformly distributed between 0 and 1, we assigned an integer i as

$$i = \text{int}[-\log(r) \times N_{bank}/2], \quad (2)$$

where the function $\text{int}[x]$ gives the integer part of x . For $i < 1$ or $i > N_{bank}$, we set $i = \text{int}[r \times N_{bank}] + 1$ by using another random number. Finally, the i th ranked conformation is selected.

In this selection rule, the higher a conformation is ranked, the more the conformation is likely to be selected. To select two different parent solutions, we simply performed the selection process twice while the second selection was repeated if it gave the identical selection of the first.

2.5.3. Mutation

The mutation of a selected parent conformation was executed by perturbing its atomic coordinates in a random fashion. Two kinds of mutation were used. The first is to relocate a single atom to prevent possible coordination defects in the unit cell. By counting the number of bonds between atoms, an atom with the largest coordination number was identified. If there were multiple such atoms, we selected one in a random fashion. Similarly, another atom with the smallest coordination number was selected. Then, the largest coordination-number atom was relocated in the neighborhood of the lowest coordination-number atom in a random fashion.

In the second mutation, multiple atoms were perturbed in a concerted fashion. We used two types of perturbation: (i) displacements of atoms by using a ripple operator [14] and (ii) movements along soft phonon modes [70–72] that were obtained from the dynamical matrix based on either a simple interatomic force model [73] or a random interaction model. The concept of soft phonon modes and their effectiveness in the global geometry optimization were demonstrated for the structure prediction of clusters [70,71] and crystals [72]. Here we adopted soft phonon modes in the mutation process of the CSA protocol.

We also perturbed the lattice parameters (a, b, c, α, β , and γ) in a random fashion, which were coupled by an appropriate uniform adjustment of all the atomic coordinates so that the unit cell is uniformly occupied by the constituting atoms. To define the amount of perturbation, we used the Gaussian distribution with the mean value of 0 and the standard deviation of 4% of the current value. For example, the lattice parameter a is perturbed by $a \rightarrow a(1 + 0.04d)$, where d is in the unit of the standard deviation of the normal distribution. In the normal distribution, the probabilities for $-1 \leq d \leq 1$, $-2 \leq d \leq 2$, and $-3 \leq d \leq 3$ are 68%, 95%, and 99.7%, respectively.

2.5.4. Crossover

The crossover operation requires two parent solutions as input. The crossover with the lattice parameters is rather straightforward since it involves just 6 parameters in one-dimensional representation. We performed either a single-point crossover or a uniform random crossover with the 50% mixing probability in Fig. 2.

The crossover with n atomic positions in the unit cell is more complicated. To perform the crossover operation, the atomic positions were represented by a one-dimensional array as follows. The coordinates of atoms were translated so that the center of mass became the coordinate origin. After three random rotations were

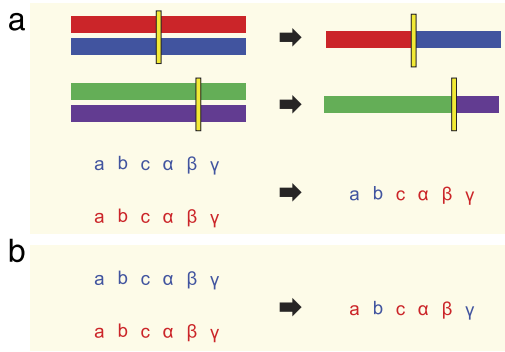


Fig. 2. (a) Illustration of the single-point crossover operation. Vertical lines represent crossover points and long horizontal bars stand for one-dimensional representation of atoms in molecules or solid systems. (b) An example of the uniform crossover operation for the lattice parameters.

executed along the z -, y -, and x -axes, the sequence of the atomic positions sorted by their x values in the ascending order became the one-dimensional representation of the atomic coordinates. With this representation, both the single-point crossover and the uniform random crossover mentioned above can be defined in a similar manner. For the single-point crossover operation, the crossover point was chosen to be positioned at 25% ~ 75% of the array.

The crossover operation can be performed either separately for the lattice parameters and atomic positions or together with all the variables. The integrity of the generated trial conformation was checked by the constraints imposed to the lattice parameters, and if violated, we discarded the conformation and repeated the crossover procedure until a viable conformation was obtained. But sometimes, for the lattice parameters, the crossover operation failed to provide a viable conformation, and in this case, we tried random generation of the lattice parameters.

2.5.5. Distance measure between two solutions

Proper definition of the distance measure between two given solutions is a critical component of the CSA algorithm. The measure should provide a quantitative number that can indicate the similarity and/or dissimilarity between two given structures. The distance measure in AMADEUS was determined by defining a bond length vector. For a given crystal structure, we took a $2 \times 2 \times 2$ expansion of the unit cell. By measuring all bond lengths and listing them in the ascending order, we constructed the bond length vector of a given crystal structure. The distance between two crystal structures is defined as the square root of the Hamming distance between their bond length vectors. Here, the Hamming distance is given by the sum of differences between the components of two vectors.

2.5.6. Local energy minimization

After trial conformations were generated, their energies were locally minimized and their objective function values were evaluated through first-principles electronic structure calculations. We employed the functional form of Perdew, Burke, and Ernzerhof (PBE) for the exchange–correlation potential [74] and the projector augmented wave pseudopotentials [75], as implemented in the VASP code [76]. The wave functions were expanded in plane waves. For the study of Si crystals, which will be discussed next, we used the kinetic energy cutoff of 400 eV and tested a higher cutoff value of 600 eV to confirm the stability of crystal structures.

Using a \bar{k} -point mesh with a grid spacing of $2\pi \times 0.08 \text{ \AA}^{-1}$, we performed an iterative procedure until all the forces and stress tensors were less than 0.01 eV/Å and 1.5 kbar, respectively. The crystal

structures were optimized by varying the lattice parameters and atomic coordinates. Such local minimized structures are at least metastable if the stability conditions are satisfied [63,64]. For selected candidate crystal structures, Kohn–Sham eigenvalues [77] were recalculated by using a higher resolution \bar{k} -point mesh than that used for the CSA search. In searching for direct band gap Si crystals, we used the fine grid spacings of $2\pi \times 0.01 \sim 2\pi \times 0.02 \text{ \AA}^{-1}$, corresponding to about 1000 ~ 2000 \bar{k} points in the irreducible Brillouin zone.

3. A case study: Design of direct gap silicon allotropes

Silicon is one of the most abundant elements on the surface of Earth and the most important material for electronic devices. However, the optical properties of cubic diamond Si (c -Si) are poor owing to its indirect band gap nature. Moreover, the large direct band gap of about 3.4 eV precludes even a sizable overlap with the solar spectrum. For potential solar cell applications, it is desirable to search for Si crystals with optically allowed direct band gaps and good lattice matching with the cubic diamond phase. Using various search methods, such as minima hopping [8,43], particle swarm optimization [15], and random structure search [5], several metastable Si crystals with direct or quasidirect band gaps have been proposed [33–36]. Although these crystals exhibit improved optical absorption properties compared with c -Si, their synthesis has yet to be explored. Recently, a metastable orthorhombic allotrope of Si, Si_{24} , has been synthesized, which has a quasidirect band gap of about 1.3 eV [78].

Two types of inverse design approaches are possible for the discovery of new photovoltaic materials. One just performs structure predictions to find the energetically favorable structures and then in a post-processing step examines whether any of the structures with reasonably low energies has interesting photovoltaic properties [32,36]. The other approach, adopted in the present work, is the inverse design approach where one tries to find directly the material with the desired electronic properties. We emphasize that our method mainly focuses on the prediction of new materials with novel functionality through the inverse design approach, in contrast with the structure search for energetically favorable structures, followed by a post-processing step of finding functional materials [32,36].

As an example of materials design, we applied our AMADEUS protocol to search for Si crystal structures with direct band gaps. This example illustrates how the CSA method works for the materials design, without using any knowledge of known crystal structures. In the following, we describe the objective function used for the design of direct band gap Si crystals.

3.1. Objective function for direct gap Si crystals

To articulate the direct gap nature of Si, we used the objective function (f_0) defined as [55],

$$f_0(E_g^d, E_g^i) = -E_g^i + \text{Max}[0, (E_g^d - E_g^i)], \quad (3)$$

where E_g^d and E_g^i denote direct and indirect band gaps, respectively. As illustrated in Fig. 3(a), the objective function favors the electronic structure with a large indirect band gap but a smaller direct band gap. We point out that Eq. (3) is just one of many choices for the objective function which can be used for the design of direct band gap semiconductors. According to the Shockley–Queisser limit [79], the optimal band gap of a semiconductor for solar cell applications is 1.1 ~ 1.3 eV. Since the band gap of Si is underestimated by about 47% with the PBE functional, the ideal band gap size will be 0.5 ~ 0.8 eV. For this purpose, one can simply add the

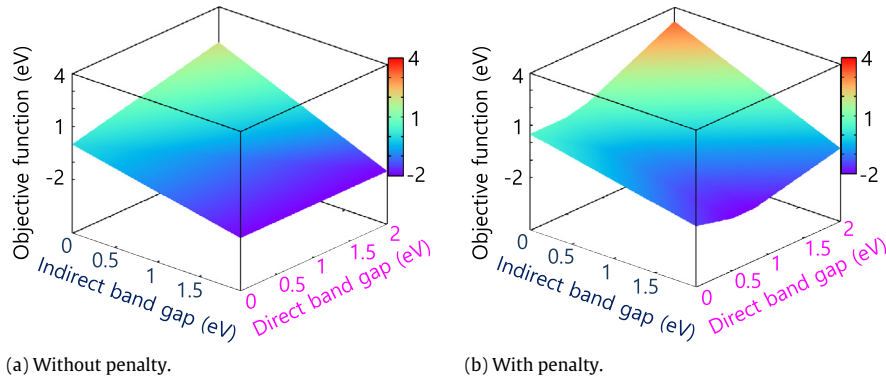


Fig. 3. Two different objective functions, (a) without penalty and (b) with penalty, as the function of both indirect and direct band gap sizes for the search of direct band gap Si crystals.

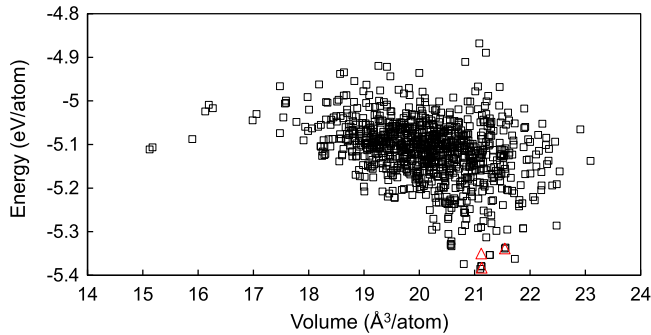


Fig. 4. Energies and volumes of the metastable structures found by our CSA approach for the Si systems with 14 atoms per unit cell. The crystal structures with direct and indirect band gaps are marked by red triangles and black squares, respectively. (For interpretation of the references to color in this figure legend, the reader is referred to the web version of this article.)

following penalty function (f_p) to the objective function of Eq. (3), which is defined as

$$f_p(E_g^d) = \begin{cases} 0.5 - E_g^d & \text{if } E_g^d < 0.5 \text{ eV,} \\ 0 & \text{if } 0.5 \leq E_g^d \leq 0.8 \text{ eV,} \\ E_g^d - 0.8 & \text{if } E_g^d > 0.8 \text{ eV.} \end{cases} \quad (4)$$

With including the penalty function, the objective function promotes the formation of direct band gaps in the range of 0.5 ~ 0.8 eV, as shown in the landscape of $f_0 + f_p$ [Fig. 3(b)].

We did not include any constraints that prevent finding very high energy structures. In our test run for systems with 14 Si atoms per unit cell, we obtained 936 metastable crystals, as shown in Fig. 4. The average volume and average energy were estimated to be 20.12 Å³/atom and -5.11 eV/atom, respectively, with their standard deviations of 1.01 Å³/atom and 0.07 eV/atom. Although the crystal structures with relatively low energies do not necessarily stand for the direct band gap nature, we successfully obtained three direct band gap allotropes (marked by red triangles in Fig. 4) with low energies out of 936 crystals. This result illustrates that our CSA approach works well for the design of direct band gap crystals, where the local enthalpy minimization process and the evaluation of the objective function value are simultaneously performed for each conformation.

3.2. Results and discussion

We considered Si crystals with even numbers of atoms per unit cell ($n = 10, 12, 14, 16, 18$, and 20). At the initial stage, $N_{\text{bank}} = 20$ solutions were chosen to constitute the sampling population, and later N_{bank} was increased to 50. Using AMADEUS based on the CSA method, we obtained a large number of local

minimum enthalpy solutions. Many promising metastable Si crystals with direct, quasidirect, and indirect band gaps were previously reported [55], including superlattice structures with direct band gaps [62]. Among these structures, the low-energy non-superlattice allotropes ($E_{\text{tot}} \leq 0.22$ eV/atom), which include 6 crystals with direct gaps, 11 with quasi-direct gaps, and 10 with indirect gaps, are listed in the Appendix. We note that any crystal structures with direct band gaps were not found in the previous work based on the low-energy structure search method [32,36]. The structural analysis was performed by examining the distributions of coordination numbers, bond lengths, bond angles, and dihedral angles from the $2 \times 2 \times 2$ expansion of the unit cell. The cutoff bond length of 2.75 Å was used to define the covalent bond.

We note that all Si atoms obtained in this study are fourfold coordinated, without any coordination defects. However, some tetrahedral bonds are distorted, leading to deviations of both bond lengths and bond angles from their ideal values. The excess energies of the obtained metastable Si allotropes range from 0.06 to 0.22 eV/atom (see Appendix). The standard deviations of bond lengths from the ideal value (σ_r) are less than 0.05 Å and those for bond angles (σ_θ) range from 8° to 15°. While the excess energy is proportional to both σ_r and σ_θ , it comes mostly from the bond angle deviation.

On the other hand, the distributions of dihedral angles from the ideal value were shown to be broadened [55], similar to the nearly flat distribution found for amorphous Si (*a*-Si) [80,81]. The structural properties of *a*-Si and amorphous SiO₂ can be described by a continuous random network (CRN) model [82,83]. The key feature of the CRN model is that the dihedral angles are rather broadly distributed, ensuring that the atom-atom positional correlation decays quickly over a short distance, without severe deviations from the ideal values for bond length and bond angle. We note that the CRN model is not the only one that can explain and fit the radial distribution function of *a*-Si [84]. As an alternative approach, a paracrystalline model was proposed and showed a good fit, in which micro-crystalline grains are surrounded by an amorphous network, thus yielding a short-range order but not a long-range order [85]. The metastable Si allotropes satisfy the key feature of the CRN model, exhibiting the short-range structural properties similar to that of *a*-Si. However, the deviations of bond lengths and bond angles are less than those ($\sigma_r = 0.09$ Å and $\sigma_\theta = 14.04^\circ$) for *a*-Si [81]. Moreover, our Si allotropes are crystalline, thus, they have a long-range order but a lack of short-range order, in contrast to the paracrystalline model. Thus, our Si allotropes belong to a special category of crystals and may provide an alternative view for the radial distribution function of *a*-Si [86].

To combine a newly designed semiconductor with a Si-based integrated circuit, a good lattice matching between the semiconductor and *c*-Si is important. In addition, for solar cell

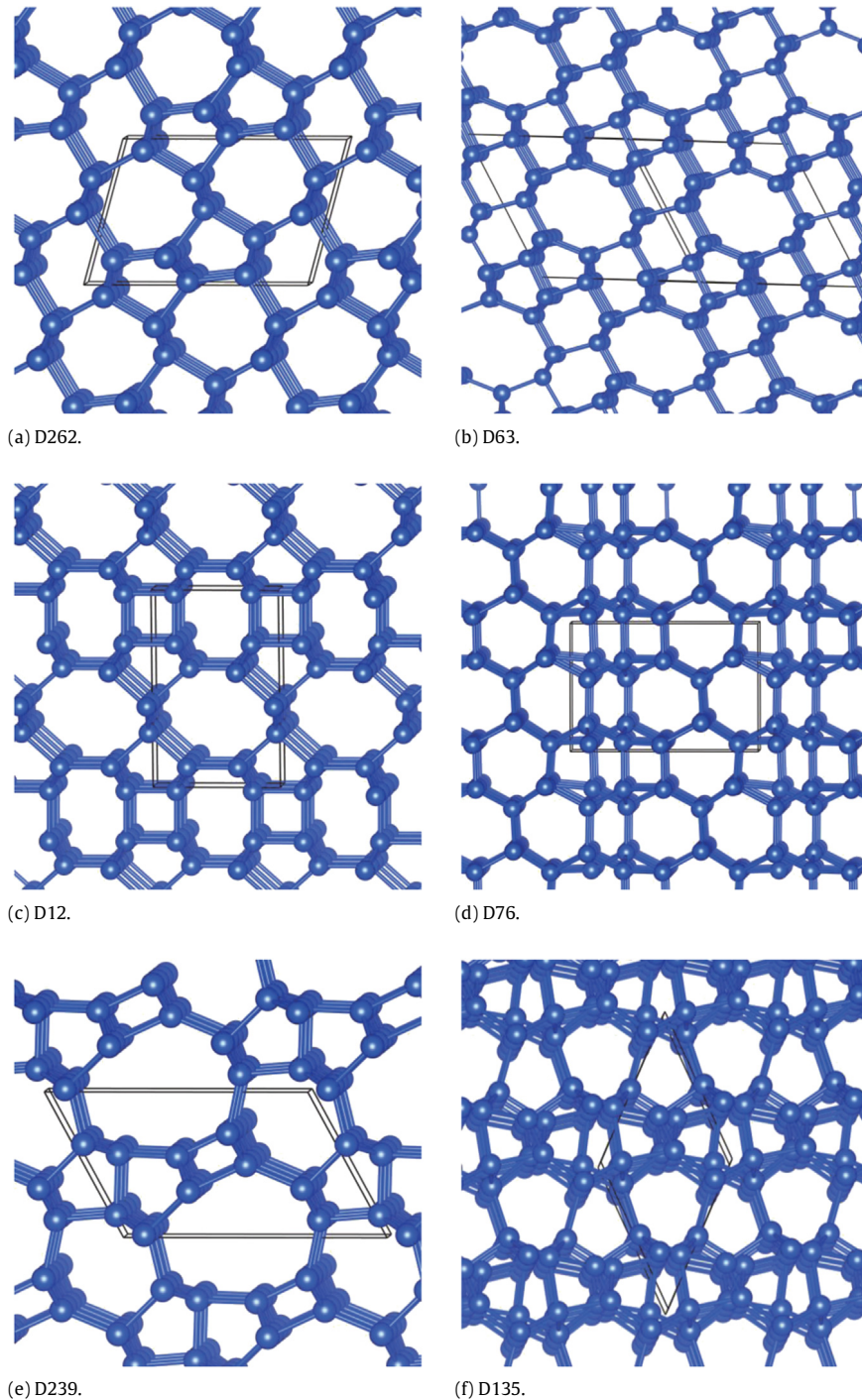


Fig. 5. Atomic structures of (a) D262, (b) D63, (c) D12, (d) D76, (e) D239, and (f) D135. Note that coordination defects do not exist. Black solid lines represent the primitive cells.

applications, it is desirable for the semiconductor to have an optically allowed direct band gap. Below, we focus on six Si crystals with direct band gaps (Table 1) for their potential applications to solar cells. The atomic structures of these six allotropes are shown in Fig. 5 and the details of structural information are given in the Appendix. We note that these structures are characterized by a mixture of 4- to 9-membered rings, while only 6-membered rings exist in c-Si.

In D262, a local configuration consisting of a pair of 5- and 7-membered rings is similar to the Stone–Wales defect in graphene [87], which is formed by rotating a bond. When all the bonds sharing adjacent 5-membered rings are properly rotated,

D262 recovers the diamond structure after constant shifts of the corresponding bonds, followed by relaxations.

In D63, two 5-membered rings also share a bond, and 8-membered rings form a hexagonal lattice between 6-membered rings. It is interesting to note that an 8-membered ring resembles a divacancy defect in the diamond lattice. In fact, D63 can be converted to the diamond structure, if two Si atoms are properly inserted in the middle of each 8-membered ring (see Appendix).

Unlike the other allotropes, D12 and D239 consist of relatively smaller and larger rings, such as 4-, 8-, and 9-membered rings. In D12, the arrangement of 4- and 8-membered rings is similar to that of Z-carbon [88,89], while 6-membered rings are absent.

Table 1
Structural and electronic properties of the direct gap Si allotropes (Ref. [55])^a.

| Structure | n | Ω_c | E_{tot} | $E_g^d(\text{PBE})$ | $E_g^d(G_0W_0)$ | Space group |
|-----------|-----|------------|-----------|---------------------|-----------------|-------------------|
| D262 | 10 | 21.02 | 0.08 | 0.29 | 0.72 | $P2_1/m$ (No. 11) |
| D63 | 12 | 21.10 | 0.12 | 0.66 | 1.07 | $C2/m$ (No. 12) |
| D12 | 10 | 21.56 | 0.13 | 0.50 | 0.93 | $Cmmm$ (No. 65) |
| D76 | 20 | 21.70 | 0.13 | 0.57 | 0.94 | $C2$ (No. 5) |
| D239 | 10 | 22.72 | 0.16 | 0.77 | 1.16 | $P1$ (No. 1) |
| D135 | 12 | 21.24 | 0.22 | 0.64 | 1.05 | Cc (No. 9) |

^a For each crystal structure, the number of atoms per unit cell (n), volume per atom (Ω_c in $\text{\AA}^3/\text{atom}$), total energy per atom (E_{tot} in eV/atom) relative to cubic diamond Si, direct band gap size (E_g^d in eV), and space group are shown. For the band gaps, the results of both the standard PBE exchange–correlation functional and quasiparticle G_0W_0 calculations are given.

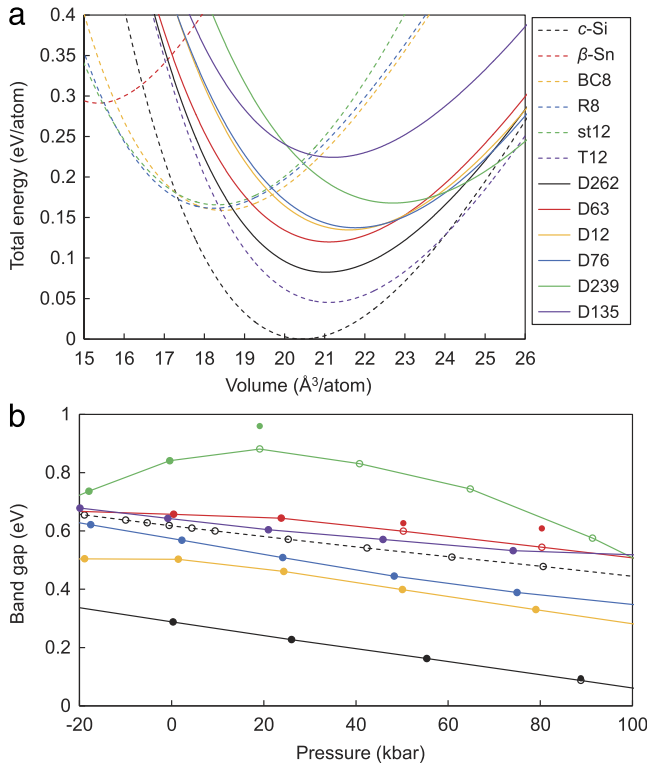


Fig. 6. (a) Energy–volume curves for D262, D63, D12, D76, D239, and D135 and comparison with those for the cubic diamond, β -Sn, BC8, R8, st12, and T12 phases of Si. (b) Band gap variations with pressure for the direct gap Si allotropes and c-Si. Filled and empty circles denote the direct and indirect band gaps, respectively.

In D76 and D135, the bond characteristics are complex because two different regions are periodically stacked. While 6-membered rings are dominant in one region, significant bond exchanges occur in the other region, resulting in a zigzag type of bond arrangement.

The total energies of the direct gap allotropes are plotted as the function of the atomic volume and compared with those for the existing Si crystals (β -Sn [90,91], BC8 [92], R8 [93], st12 [94], T12 [95], and cubic diamond) in Fig. 6(a). We find that the energies of D262, D63, D12, and D76 are lower than those for BC8, R8, and st12. It is known that c -Si undergoes a structural transformation to the metallic β -Sn phase under high pressure [90,91]. Upon slow pressure release from the β -Sn phase, instead of returning to the most stable diamond phase, Si transforms to the BC8 and/or R8 phase with the distorted tetrahedral bonding [92,93]. Moreover, the hexagonal diamond (lonsdaleite) phase and/or the T12 (Si-XIII) structure can be formed by annealing the BC8 and/or R8 phase at ambient pressure [92,95–97]. Recently, it was reported that ultrashort laser-induced microexplosion can produce the metastable st12 phase in a confined region of Si [94]. Using a similar annealing process for the metastable BC8 and/or R8 phase or a microexplosion technique that induces non-equilibrium

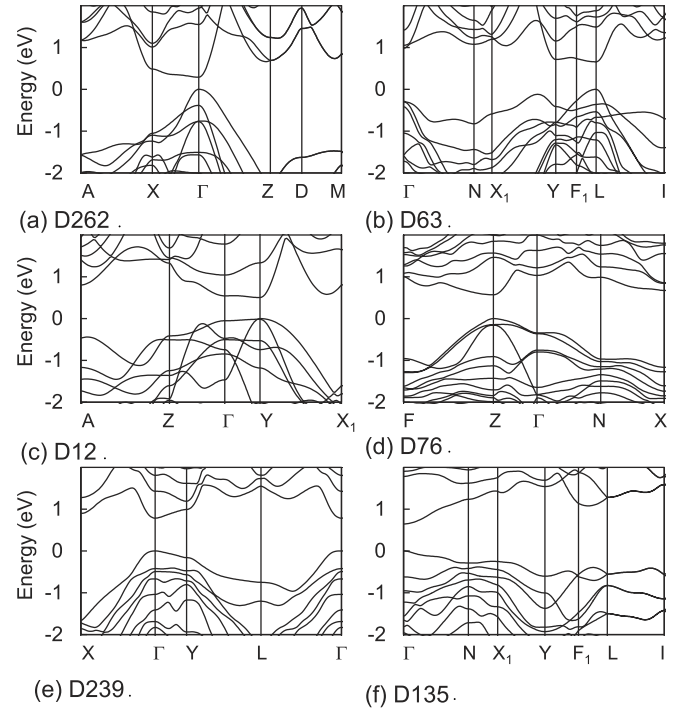


Fig. 7. Band structures of (a) D262, (b) D63, (c) D12, (d) D76, (e) D239, and (f) D135 calculated by using the PBE functional. The valence band maximum is set to zero in energy.

states, it might be possible to form the low-energy allotropes, especially, D262 and D63. While the equilibrium volumes of β -Sn, BC8, R8, and st12 are smaller than that of c -Si, those of the direct gap allotropes obtained in this study are all larger by 3% ~ 11%, resulting in lower atomic densities. We note that the lattice mismatches are rather small (1% ~ 4%), indicating that, if one of these crystals is realized by experiment, it can be readily combined with the existing Si-based technology.

The structure stability of the allotropes at the ambient condition was examined in two ways. Firstly, we carried out first-principles lattice dynamics calculations [98]. The dynamical matrices were calculated by employing the $2 \times 2 \times 2$ supercells for D262, D63, D12, and D135, the $3 \times 3 \times 2$ supercell for D76, and the $2 \times 3 \times 2$ supercell for D239. We found no imaginary phonon modes in the Brillouin zone, confirming that all six direct gap allotropes are dynamically stable. Secondly, we performed first-principles molecular dynamics simulations for 20 ps to examine the thermal stability. While D135 was shown to transform into Q135 upon annealing above 500 K [55], the other five direct gap allotropes were stable at temperatures up to 800 K.

The band structures of the six direct gap allotropes are shown in Fig. 7. The direct band gaps are found at the Γ point for D262, D239, and D135, whereas those for D63, D12, and D76 are located

Table 2Calculated photovoltaic performance of the direct gap allotropes in Table 1^a.

| Structure | Type | $E_{G_0W_0-BSE}^{(d)}$ | $E_{G_0W_0-BSE}^{(da)}$ | f_r | L | V_{oc} | V_{max} | SLME(%) | Ref. |
|-----------|------|------------------------|-------------------------|----------------------|-----|----------|-----------|---------|------|
| D262 | OT1 | 0.64 | 0.64 | 1.00 | 0.5 | 0.45 | 0.38 | 16.30 | |
| D63 | OT1 | 1.01 | 1.01 | 1.00 | 0.5 | 0.78 | 0.69 | 29.17 | [55] |
| D12 | OT2 | 0.83 | 0.86 | 0.28 | 0.5 | 0.59 | 0.51 | 22.54 | |
| D76 | OT1 | 0.86 | 0.86 | 1.00 | 0.5 | 0.65 | 0.57 | 22.97 | |
| D239 | OT2 | 0.74 | 0.93 | 6.5×10^{-4} | 0.5 | 0.35 | 0.29 | 12.43 | |
| D135 | OT1 | 0.98 | 0.98 | 1.00 | 0.5 | 0.75 | 0.67 | 29.71 | [55] |

^a The optical type, band gap, fraction of radiative electron–hole recombination current parameter (f_r), film thickness (L in μm), open circuit voltage (V_{oc} in volt), voltage at the maximum power (V_{max} in volt), and SLME are compared. The direct transition gap and the dipole allowed transition gap, which are denoted as $E_{G_0W_0-BSE}^{(d)}$ and $E_{G_0W_0-BSE}^{(da)}$ in units of eV, respectively, are derived from the G_0W_0 and BSE calculations.

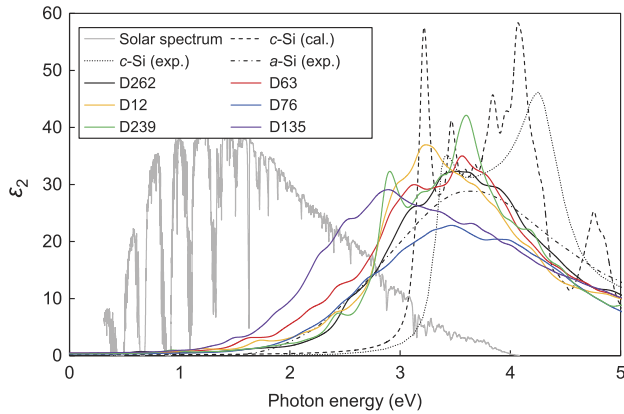


Fig. 8. Calculated imaginary parts of the dielectric function as a function of photon energy for D262, D63, D12, D76, D239, and D135 and comparison with the solar spectrum and the experimental data [102] for *c*-Si and *a*-Si.

at less symmetric points in the Brillouin zone. With the PBE exchange–correlation functional, we obtained the smallest band gap of 0.29 eV for D262, which has the highest atomic density among six. For the other five with the lower atomic densities than that of D262, the band gap sizes are in the range of 0.50 ~ 0.77 eV, exhibiting a tendency to increase with decreasing the atomic density. When more rigorous quasiparticle G_0W_0 calculations [99,100] were performed, the direct band gap nature did not change for all six allotropes, and the band gaps sizes were improved to 0.72 ~ 1.16 eV, some reaching the optimal value of solar cell applications.

The variations of the band gaps with pressure are shown for the six direct gap allotropes and compared with that of *c*-Si in Fig. 6(b). For all the allotropes, the band gap nature changes from direct to indirect as the pressure increases. In this case, the transition pressure appears to anti-correlate with the size of the direct band gap. For D239 with the largest band gap, the direct band gap initially increases up to a pressure around 10 kbar, where the direct-to-indirect gap transition occurs, and then decreases at higher pressures. The transition pressures exceed 80 kbar for D262, D12, and D76 which have relatively smaller band gaps. With the exception of D239, the band gap size tends to decrease with increasing pressure. As compared to *c*-Si, the pressure variations of the direct band gaps are smaller for D63 and D135 with the large band gaps, whereas those for the smaller gap allotropes are slightly larger. In *c*-Si, the conduction band minimum (CBM) state is located at the Δ valleys in the Brillouin zone and characterized by the charge distribution in the anti-bonding region of 6-membered rings. In the six allotropes, the CBM state of *c*-Si is not folded to the center of the Brillouin zone, where the direct band gaps occur, and the charge densities for the CBM state are mostly distributed near the 4- and 5-membered rings, where the tetrahedral bonds are severely distorted. Moreover, since the six allotropes exhibit the direct-to-indirect gap transition upon pressure, the possibility that the direct gap nature results from the folding of the Brillouin zone is ruled out.

Next, we investigated the optical absorption properties of the direct gap allotropes. We calculated the imaginary part of the dielectric function $\epsilon_2(\omega)$ by solving the Bethe–Salpeter equation (BSE) [101] together with quasiparticle G_0W_0 approximation [99,100]. Thus, the optical absorption spectrum includes electron–hole interactions. From the G_0W_0 and BSE calculations, we estimated the direct transition gap and the dipole-allowed transition gap, which are denoted as $E_{G_0W_0-BSE}^{(d)}$ and $E_{G_0W_0-BSE}^{(da)}$, respectively. The results for $\epsilon_2(\omega)$ are shown in Fig. 8, along with the solar spectrum and the measured dielectric functions for *c*-Si and *a*-Si [102]. Owing to the direct band gaps around 1 eV, the overlap of the absorption spectrum with the solar spectrum is much enhanced for D63 and D135, compared with *c*-Si. Especially, the absorption spectra of D63 and D135 significantly overlap with the solar spectrum, whereas those for D262, D12, D76, and D239 are comparable to that of *a*-Si.

The enhanced overlap with the solar spectrum alone cannot justify the usefulness of the designed allotropes. We examined the photovoltaic efficiency in terms of spectroscopic limited maximum efficiency (SLME) [37], which takes into account the band gap, the shape of absorption spectrum, and the nonradiative recombination loss. The evaluation of SLME based on first-principles spectroscopy calculations is a generalized version of the Shockley–Queisser limit [79] for the photovoltaic efficiency. The power conversion efficiency of a thin film solar-cell depends on the fraction of radiative electron–hole recombination current (f_r) and the photon absorptivity. In addition, the film thickness (L) is explicitly taken into account. While the solar-cell efficiency depends on the gap size, it is irrelevant to whether the band gap is direct or indirect [79].

The classification of photovoltaic materials into four optical types (OT1, OT2, OT3, and OT4) was suggested, based on the relative orders of dipole-allowed, dipole-forbidden, and indirect transitions [37]. In OT1, the dipole-allowed direct gap corresponds to the lowest energy transition, whereas the next transition above it is direct but dipole-forbidden. On the other hand, the lowest energy transition is direct but dipole-forbidden in OT2, while OT3 and OT4 are the optical types of indirect gap materials. The six direct gap allotropes found in this study are of only two types: OT1 for D262, D63, D76, and D135; OT2 for D12 and D239 (Table 2). In solar cells made from direct gap materials such as CdTe, CIGS, and CZTS, light can be efficiently absorbed even with thin films of $\sim 1 \mu\text{m}$ thickness. The calculated SLME values for the film thickness of $L = 0.5 \mu\text{m}$ are shown in Table 2. The Shockley–Queisser limit is 33.7% for the photovoltaic efficiency under the AM1.5G solar spectrum [103] with the optimal band gap of 1.34 eV. The SLME value of D262 with the smallest band gap is quite low, around 16%. In D239, which belongs to the OT2 type, with the large difference between $E_{G_0W_0-BSE}^{(d)}$ and $E_{G_0W_0-BSE}^{(da)}$, its SLME value is only about 12%, lowest among the six allotropes. On the other hand, the SLME values of D63 and D135 reach about 30%, indicating that their photovoltaic efficiencies are comparable to those of best-known photovoltaic materials such as CuInTe₂, CuInSe₂, AgInTe₂, AgInSe₂, and CuGaSe₂ [37].

Table A.1

Summary of the structural and electronic properties of the metastable Si allotropes. For each crystal structure, the number of atoms per unit cell (n), volume per atom (Ω_c in $\text{\AA}^3/\text{atom}$), total energy per atom (E_{tot} in eV/atom) relative to cubic diamond Si, direct band gap size (E_g^d in eV), and indirect band gap size (E_g^i in eV), and space group are shown. For the band gaps, the results of both the standard PBE exchange–correlation functional and quasiparticle G_0W_0 calculations are given.

| Structure | n | Ω_c | E_{tot} | $E_g^d(\text{PBE})$ | $E_g^i(\text{PBE})$ | $E_g^d(G_0W_0)$ | $E_g^i(G_0W_0)$ | Space group | Ref. |
|--------------|-----|------------|------------------|---------------------|---------------------|-----------------|-----------------|-------------------------------|------|
| D262 | 10 | 21.02 | 0.08 | 0.29 | | 0.72 | | $P2_1/m(\text{No. } 11)$ | [55] |
| D63 | 12 | 21.10 | 0.12 | 0.66 | | 1.07 | | $C2/m(\text{No. } 12)$ | [55] |
| D12 | 10 | 21.56 | 0.13 | 0.50 | | 0.93 | | $Cmmm(\text{No. } 65)$ | [55] |
| D76 | 20 | 21.70 | 0.13 | 0.57 | | 0.94 | | $C2(\text{No. } 5)$ | [55] |
| D239 | 10 | 22.72 | 0.16 | 0.77 | | 1.16 | | $P1(\text{No. } 1)$ | [55] |
| D135 | 12 | 21.24 | 0.22 | 0.64 | | 1.05 | | $Cc(\text{No. } 9)$ | [55] |
| Q130 | 12 | 21.86 | 0.08 | 0.64 | 0.63 | 1.23 | 1.22 | $C2/m(\text{No. } 12)$ | [55] |
| Q78 | 20 | 21.64 | 0.11 | 0.74 | 0.69 | 1.14 | 1.09 | $Pma2(\text{No. } 28)$ | [55] |
| Q465 | 12 | 21.85 | 0.13 | 1.25 | 1.23 | 1.78 | 1.71 | $P\bar{1}(\text{No. } 2)$ | [55] |
| Q1102 | 12 | 21.55 | 0.14 | 1.33 | 1.20 | 1.78 | 1.62 | $Pc(\text{No. } 7)$ | [55] |
| Q135 | 12 | 20.89 | 0.15 | 0.93 | | 1.41 | 1.32 | $C2/c(\text{No. } 15)$ | [55] |
| Q636 | 20 | 20.89 | 0.15 | 0.96 | 0.84 | 1.37 | 1.23 | $P1(\text{No. } 1)$ | [55] |
| Q736 | 20 | 22.25 | 0.16 | 0.92 | 0.78 | 1.35 | 1.16 | $P1(\text{No. } 1)$ | [55] |
| Q419 | 12 | 20.11 | 0.20 | 1.26 | 1.11 | 1.71 | 1.55 | $P1(\text{No. } 1)$ | [55] |
| Q85 | 20 | 20.43 | 0.21 | 0.69 | 0.58 | 0.99 | 0.95 | $P1(\text{No. } 1)$ | [55] |
| Q7 | 20 | 20.13 | 0.22 | 0.54 | 0.44 | 0.85 | 0.75 | $P1(\text{No. } 1)$ | [55] |
| Q202 | 20 | 21.73 | 0.22 | 0.47 | 0.43 | 0.73 | | $P1(\text{No. } 1)$ | [55] |
| I1373 | 14 | 20.61 | 0.06 | 1.66 | 1.29 | 2.08 | 1.75 | $I\bar{4}(\text{No. } 82)$ | [55] |
| I926 | 16 | 20.72 | 0.07 | 1.31 | 1.10 | 1.77 | 1.47 | $C2/m(\text{No. } 12)$ | [55] |
| I1229 | 16 | 22.29 | 0.11 | 0.89 | 0.62 | 1.35 | 1.05 | $P\bar{1}(\text{No. } 2)$ | [55] |
| I16 | 20 | 20.68 | 0.12 | 0.92 | 0.68 | 1.36 | 1.14 | $P2_1(\text{No. } 4)$ | [55] |
| I391 | 12 | 20.58 | 0.12 | 1.09 | 0.91 | 1.60 | 1.31 | $P2_1/m(\text{No. } 11)$ | [55] |
| I671 | 18 | 22.61 | 0.14 | 1.34 | 0.97 | 0.93 | 0.72 | $P1(\text{No. } 1)$ | [55] |
| I257 | 20 | 20.76 | 0.16 | 0.80 | 0.63 | 1.18 | 0.97 | $P1(\text{No. } 1)$ | [55] |
| I512 | 12 | 22.61 | 0.16 | 1.12 | 0.95 | 1.66 | 1.31 | $Pm(\text{No. } 6)$ | [55] |
| I1233 | 16 | 20.76 | 0.16 | 1.00 | 0.69 | 1.39 | 1.11 | $P1(\text{No. } 1)$ | [55] |
| I241 | 12 | 18.33 | 0.18 | 1.08 | 0.85 | 1.46 | 1.24 | $P2_1/c(\text{No. } 14)$ | [55] |
| α -Si | | | 0.28 | | | | | | [80] |
| α -Si | | | 0.25 | | | | | | [81] |
| c-Si | 2 | 20.46 | 0.00 | 2.56 | 0.62 | 3.21 | 1.14 | $Fd\bar{3}m(\text{No. } 227)$ | |

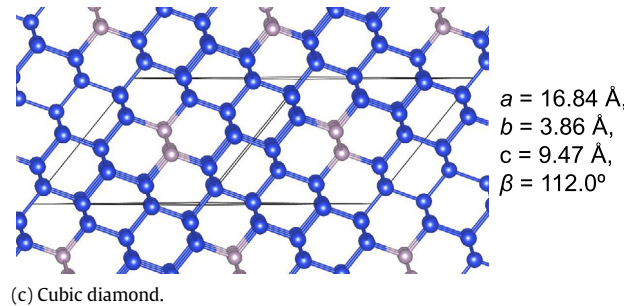
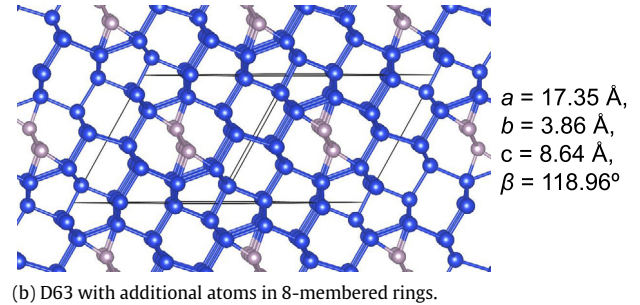
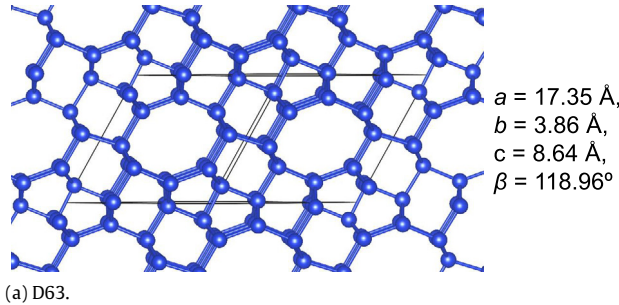


Fig. A.1. Structural transformation of Si from the D63 to cubic diamond structure after adding two Si atoms in the middle of each 8-membered ring and subsequent lattice relaxations.

4. Conclusion

We have developed a protocol for computational materials design, called AMADEUS, in which the CSA algorithm for global optimization is combined with first-principles DFT calculations. We used a variant of CSA, in which the local energy/enthalpy minimization of trial solutions is performed and their objective

function values are evaluated from first-principles calculations. The goal of AMADEUS was set to obtain as many distinct solutions as possible not just the most optimal solution. We have demonstrated the utility of AMADEUS for first-principles materials design by applying it to the design of direct band gap Si crystals. The optical properties of the designed Si crystals with direct band gaps were examined, and some of them stood out as

Table A.2

Space groups and lattice parameters of the direct band gap Si allotropes of D262, D63, D12, D76, D239, and D135.

| Structure | Space group | <i>a</i> (Å) | <i>b</i> (Å) | <i>c</i> (Å) | α (°) | β (°) | γ (°) | Ref. |
|-----------|---|--------------|--------------|--------------|--------------|-------------|--------------|------|
| D262 | <i>P</i> 2 ₁ / <i>m</i> (No. 11) | 6.17 | 3.87 | 9.13 | 90.00 | 104.90 | 90.00 | |
| D63 | <i>C</i> 2/ <i>m</i> (No. 12) | 17.35 | 3.86 | 8.64 | 90.00 | 118.96 | 90.00 | |
| D12 | <i>Cmmm</i> (No. 65) | 3.87 | 18.70 | 5.95 | 90.00 | 90.00 | 90.00 | |
| D76 | <i>C</i> 2 (No. 5) | 9.41 | 9.46 | 9.74 | 90.00 | 90.26 | 90.00 | |
| D239 | <i>P</i> 1 (No. 1) | 6.47 | 3.85 | 9.31 | 89.44 | 78.39 | 89.96 | |
| D135 | <i>Cc</i> (No. 9) | 13.88 | 5.69 | 7.10 | 90.00 | 114.64 | 90.00 | [55] |

Table A.3

Wyckoff positions of the direct band gap Si allotropes of D262, D63, D12, D76, D239, and D135 [55].

| Structure | Wyckoff positions |
|-----------|--|
| D262 | 2e (0.88644, 0.25, 0.50524) 2e (0.58747, 0.25, 0.06048) 2e (0.69322, 0.25, 0.70270) 2e (0.89630, 0.25, −0.03566) 2e (0.54243, 0.25, 0.30946) |
| D63 | 4i (0.68961, 0, 0.16485) 4i (0.58021, 0, 0.54818) 4i (0.15541, 0, 0.71270) 4i (0.14836, 0, −0.02151) 4i (0.41673, 0, 0.72407) 4i (−0.00288, 0, 0.86420) |
| D12 | 4i (0, 0.21409, 0) 8n (0, 0.56359, 0.19893) 8n (0, 0.12851, 0.29982) |
| D76 | 4c (0.73783, 0.01757, 0.28978) 4c (0.83237, 0.08718, 0.88688) 4c (0.82252, 0.10221, 0.50603) 4c (0.41784, 0.33536, 0.28760) 4c (0.24639, 0.17455, 0.89651) 4c (0.42606, 0.35448, −0.09903) 4c (0.32641, 0.10542, 0.30103) 4c (0.00673, 0.42799, 0.30390) 4c (0.01641, 0.26900, 0.87937) 2b (0, −0.07570, 0.5) 2b (0, 0.28236, 0.5) |
| D239 | 1a (0.81487, 0.13866, 0.61541) 1a (0.11402, 0.56696, 0.36163) 1a (0.02448, 0.63805, 0.62880) 1a (0.39896, 0.58640, −0.06132) 1a (0.57857, 0.08917, 0.83756) 1a (0.06387, 0.58259, 0.88030) 1a (0.44285, 0.58574, 0.19180) 1a (0.86355, 0.08075, −0.03945) 1a (0.65678, 0.08484, 0.19904) 1a (0.89641, 0.06728, 0.35819) |
| D135 | 4a (0.76151, 0.22554, 0.81502) 4a (0.51344, 0.35694, 0.33621) 4a (−0.02003, 0.45610, 0.25093) 4a (0.08246, 0.15420, 0.20316) 4a (0.86488, 0.42773, 0.41962) 4a (0.32774, 0.41392, 0.07504) |

excellent potential candidates for solar-cell applications, with the photovoltaic efficiencies comparable to those of best-known non-silicon photovoltaic materials.

Although AMADEUS was applied for the structure search of direct band gap Si crystals, its application can be easily extended to other types of materials design once the problem-dependent objective function is articulated. The current version of AMADEUS utilizes only the core ingredients of CSA, and it is straightforward to incorporate the full features of CSA, which can improve the search efficiency even further. Although the first-principles DFT calculations are computationally intensive, we can implement the parallel-in-parallel scheme in AMADEUS, which allows us to utilize

thousands of CPU cores efficiently. Thus, we hope that AMADEUS can expedite the progress of the materials design in near future.

Acknowledgments

IHL and JL* (jlee@kias.re.kr) were supported by the National Research Foundation of Korea (NRF) under Grant No. 2008-0061987 funded by the Korea government (MEST). IHL, YJO, SK, and KJC* (kjchang@kaist.ac.kr) were supported by Samsung Science and Technology Foundation under Grant No. SSTF-BA1401-08. We thank Korea Institute for Advanced Study (KIAS Center for Advanced Computation) for providing computing resources.

Appendix

The structural and electronic properties of the metastable Si allotropes with the low energies ($E_{tot} \leq 0.22$ eV/atom) are compared in Table A.1. The crystal information on the space groups, lattice parameters, and Wyckoff positions of the six direct gap allotropes is given in Tables A.2 and A.3. The structural transformation from D63 to cubic diamond Si by adding two Si atoms at the center of each 8-membered ring is atomically visualized in Fig. A.1.

References

- [1] P. Hohenberg, W. Kohn, Phys. Rev. 136 (1964) B864–B871.
- [2] A. Franceschetti, A. Zunger, Nature 402 (1999) 60–63 London.
- [3] S.M. Woodley, R. Catlow, Nature Mater. 7 (2008) 937–946.
- [4] J.C. Schön, K. Doll, M. Jansen, Phys. Status Solidi b 247 (2010) 23–39.
- [5] C.J. Pickard, R.J. Needs, J. Phys.: Condens. Matter 23 (2011) 053201.
- [6] A.R. Oganov (Ed.), Modern Methods of Crystal Structure Prediction, Wiley-VCH Verlag GmbH & Co, KGaA, Weinheim, Germany, 2010.
- [7] C.W. Glass, A.R. Oganov, N. Hansen, Comput. Phys. Commun. 175 (2006) 713–720.
- [8] N.L. Abraham, M.I.J. Probert, Phys. Rev. B 73 (2006) 224104.
- [9] G. Trimarchi, A. Zunger, Phys. Rev. B 75 (2007) 104113.
- [10] S.M. Woodley, C.R.A. Catlow, Comput. Mater. Sci. 45 (2009) 84–95.
- [11] C.E. Mohn, W. Kob, Comput. Mater. Sci. 45 (2009) 111–117.
- [12] M. Amsler, S. Goedecker, J. Chem. Phys. 133 (2010) 224104.
- [13] A. Fadda, G. Fadda, Phys. Rev. B 82 (2010) 104105.
- [14] D.C. Lonie, E. Zurek, Comput. Phys. Commun. 182 (2011) 372–387.
- [15] Y. Wang, J. Lv, L. Zhu, Y. Ma, Comput. Phys. Commun. 183 (2012) 2063–2070.
- [16] S. Curtarolo, W. Setyawan, G.L.W. Hart, M. Jahnatek, R.V. Chepulskii, R.H. Taylor, et al., Comput. Mater. Sci. 58 (2012) 218–226.
- [17] Y.-Y. Zhang, W. Gao, S. Chen, H. Xiang, X.-G. Gong, Comput. Mater. Sci. 98 (2015) 51–55.
- [18] Q. Li, D. Zhou, W. Zheng, Y. Ma, C. Chen, Phys. Rev. Lett. 110 (2013) 136403.
- [19] B. Meredig, C. Wolverton, Nature Mater. 12 (2013) 123–127.
- [20] S. Curtarolo, G.L.W. Hart, M.B. Nardelli, N. Mingo, S. Sanvito, O. Levy, Nature Mater. 12 (2013) 191–201.
- [21] P. Piquini, P.A. Graf, A. Zunger, Phys. Rev. Lett. 100 (2008) 186403.
- [22] A.R. Oganov, A.O. Lyakhov, M. Valle, Acc. Chem. Res. 44 (2011) 227–237.
- [23] G.H. Jóhannesson, T. Bligaard, A.V. Ruban, H.L. Skriver, K.W. Jacobsen, J.K. Nørskov, Phys. Rev. Lett. 88 (2002) 255506.
- [24] K. Kim, P.A. Graf, W.B. Jones, J. Comput. Phys. 208 (2005) 735–760.
- [25] S.V. Dudiy, A. Zunger, Phys. Rev. Lett. 97 (2006) 046401.
- [26] J. Íñiguez, L. Bellaiche, Phys. Rev. Lett. 87 (2001) 095503.
- [27] P. Piquini, A. Zunger, Phys. Rev. B 78 (2008) 161302.
- [28] K. Yang, W. Setyawan, S. Wang, M.B. Nardelli, S. Curtarolo, Nature Mater. 11 (2012) 614–619.
- [29] P. Norouzzadeh, C.W. Myles, D.J. Vashaee, Phys.: Condens. Matter 25 (2013) 475502.
- [30] G. Gao, A.R. Oganov, P. Li, Z. Li, H. Wang, T. Cui, et al., Proc. Natl. Acad. Sci. USA 107 (2010) 1317–1320.
- [31] G. Gao, A.R. Oganov, A. Bergara, M. Martinez-Canales, T. Cui, T. Iitaka, et al., Phys. Rev. Lett. 101 (2008) 107002.

- [32] S. Botti, J.A. Flores-Livas, M. Amsler, S. Goedecker, M.A.L. Marques, *Phys. Rev. B* 86 (2012) 121204.
- [33] H.J. Xiang, B. Huang, E. Kan, S.-H. Wei, X.-G. Gong, *Phys. Rev. Lett.* 110 (2013) 118702.
- [34] Q. Wang, B. Xu, J. Sun, H. Liu, Z. Zhao, D. Yu, et al., *J. Am. Chem. Soc.* 136 (2014) 9826–9829.
- [35] A. Mujica, C.J. Pickard, R.J. Needs, *Phys. Rev. B* 91 (2015) 214104.
- [36] M. Amsler, S. Botti, M.A.L. Marques, T.J. Lenosky, S. Goedecker, *Phys. Rev. B* 92 (2015) 014101.
- [37] L. Yu, A. Zunger, *Phys. Rev. Lett.* 108 (2012) 068701.
- [38] B.V.C. Martins, G. Brunetto, F. Sato, V.R. Coluci, D.S. Galvão, *Chem. Phys. Lett.* 453 (2008) 290–295.
- [39] Q. Li, H. Liu, D. Zhou, W. Zheng, Z. Wu, Y. Ma, *Phys. Chem. Chem. Phys.* 14 (2012) 13081–13087.
- [40] S. Kirkpatrick, C.D. Gelatt Jr., M.P. Vecchi, *Science* 220 (1983) 671–680.
- [41] J. Pannetier, J. Bassasalsina, J. Rodriguez-Carvajal, V. Caignaert, *Nature* 346 (1990) 343–345 London.
- [42] D.J. Wales, J.P.K. Doye, *J. Phys. Chem. A* 101 (1997) 5111–5116.
- [43] S. Goedecker, *J. Chem. Phys.* 120 (2004) 9911–9917.
- [44] R. Martoňák, D. Donadio, A.R. Oganov, M. Parrinello, *Nature Mater.* 5 (2006) 623–626.
- [45] J.H. Holland, *Adaptation in Natural and Artificial Systems*, MIT press, Cambridge, MA, 1992.
- [46] D.M. Deaven, K.M. Ho, *Phys. Rev. Lett.* 75 (1995) 288–291.
- [47] J. Kennedy, R. Eberhart, Particle swarm optimization, in: *Proc. ICNN'95 - Int. Conf. Neural Networks*, IEEE, 1995, pp. 1942–1948. <http://dx.doi.org/10.1109/ICNN.1995.488968>.
- [48] E. Bonabeau, M. Dorigo, G. Theraulaz, *Swarm Intelligence: From Natural to Artificial Systems*, Oxford University Press, New York, 1999.
- [49] E. Bonabeau, M. Dorigo, G. Theraulaz, *Nature* 406 (2000) 39–42 London.
- [50] J. Lee, H.A. Scheraga, S. Rackovsky, *J. Comput. Chem.* 18 (1997) 1222–1232.
- [51] J. Lee, I.-H. Lee, J. Lee, *Phys. Rev. Lett.* 91 (2003) 080201.
- [52] S.-Y. Kim, S.J. Lee, J. Lee, *J. Chem. Phys.* 119 (2003) 10274–10279.
- [53] K. Lee, C. Czaplewski, S.-Y. Kim, J. Lee, *J. Comput. Chem.* 26 (2005) 78–87.
- [54] S.-Y. Kim, S.B. Lee, J. Lee, *Phys. Rev. E* 72 (2005) 011916.
- [55] I.-H. Lee, J. Lee, Y.J. Oh, S. Kim, K.J. Chang, *Phys. Rev. B* 90 (2014) 115209.
- [56] F.H. Stillinger, *Phys. Rev. E* 59 (1999) 48–51.
- [57] J. Lee, J. Lee, T.N. Sasaki, M. Sasai, C. Seok, J. Lee, *Proteins: Struct., Funct., Bioinf.* 79 (2011) 2403–2417.
- [58] K. Joo, J. Lee, S. Lee, J.H. Seo, S.J. Lee, J. Lee, *Proteins: Struct., Funct., Bioinf.* 69 (2007) 83–89.
- [59] K. Joo, J. Lee, J.-H. Seo, K. Lee, B.-G. Kim, J. Lee, *Proteins: struct., Funct., Bioinf.* 75 (2009) 1010–1023.
- [60] K. Joo, J. Lee, S. Sim, S.Y. Lee, K. Lee, S. Heo, et al., *Proteins: Struct., Funct., Bioinf.* 82 (2014) 188–195.
- [61] J. Lee, S.P. Gross, J. Lee, *Phys. Rev. E* 85 (2012) 056702.
- [62] Y.J. Oh, I.-H. Lee, S. Kim, J. Lee, K.J. Chang, *Sci. Rep.* 5 (2015) 18086.
- [63] O.H. Nielsen, R.M. Martin, *Phys. Rev. Lett.* 50 (1983) 697–700.
- [64] I.-H. Lee, S.-G. Lee, K.J. Chang, *Phys. Rev. B* 51 (1995) 14697–14700.
- [65] G.J. Snyder, E.S. Toberer, *Nature Mater.* 7 (2008) 105–114.
- [66] C.J. Pickard, R.J. Needs, *Phys. Rev. Lett.* 97 (2006) 045504.
- [67] J. Lee, J. Pillardy, C. Czaplewski, Y. Arnautova, D.R. Ripoll, A. Liwo, et al., *Comput. Phys. Commun.* 128 (2000) 399–411.
- [68] K. Cahill, *Physical Mathematics*, Cambridge University Press, Cambridge, England, 2013 (Chapter 14.4).
- [69] L. Devroye, *Non-Uniform Random Variate Generation*, Springer-Verlag, New York, 1986.
- [70] S.E. Schönborn, S. Goedecker, S. Roy, A.R. Oganov, *J. Chem. Phys.* 130 (2009) 144108.
- [71] M. Sicher, S. Mohr, S. Goedecker, *J. Chem. Phys.* 134 (2011) 044106.
- [72] A.O. Lyakhov, A.R. Oganov, H.T. Stokes, Q. Zhu, *Comput. Phys. Commun.* 184 (2013) 1172–1182.
- [73] M.M. Tirion, *Phys. Rev. Lett.* 77 (1996) 1905–1908.
- [74] J.P. Perdew, K. Burke, M. Ernzerhof, *Phys. Rev. Lett.* 77 (1996) 3865–3868.
- [75] G. Kresse, D. Joubert, *Phys. Rev. B* 59 (1999) 1758–1775.
- [76] G. Kresse, J. Furthmüller, *Comput. Mater. Sci.* 6 (1996) 15–50.
- [77] W. Kohn, L.J. Sham, *Phys. Rev.* 140 (1965) A1133–A1138.
- [78] D.Y. Kim, S. Stefanoski, O.O. Kurakevych, T.A. Strobel, *Nature Mater.* 14 (2014) 169–173.
- [79] W. Shockley, H.J. Queisser, *J. Appl. Phys.* 32 (1961) 510–519.
- [80] I. Štich, R. Car, M. Parrinello, *Phys. Rev. B* 44 (1991) 11092–11104.
- [81] I.-H. Lee, K.J. Chang, *Phys. Rev. B* 50 (1994) 18083–18089.
- [82] W.H. Zachariasen, *J. Am. Chem. Soc.* 54 (1932) 3841–3851.
- [83] D.E. Polk, *J. Non-Cryst. Solids* 5 (1971) 365–376.
- [84] M.M.J. Treacy, K.B. Borisenko, *Science* 335 (2012) 950–953.
- [85] P.M. Voyles, N. Zotov, S.M. Nakhmanson, D.A. Drabold, J.M. Gibson, M.M.J. Treacy, et al., *J. Appl. Phys.* 90 (2001) 4437–4451.
- [86] J. Fortner, J.S. Lannin, *Phys. Rev. B* 39 (1989) 5527–5530.
- [87] A.J. Stone, D.J. Wales, *Chem. Phys. Lett.* 128 (1986) 501–503.
- [88] D. Selli, I.A. Baburin, R. Martoňák, S. Leoni, *Phys. Rev. B* 84 (2011) 161411(R).
- [89] M. Amsler, J.A. Flores-Livas, L. Lehtovaara, F. Balima, S.A. Ghasemi, D. Machon, et al., *Phys. Rev. Lett.* 108 (2012) 065501.
- [90] J.C. Jamieson, *Science* 139 (1963) 762–764.
- [91] J.Z. Hu, L.D. Merkle, C.S. Menoni, I.L. Spain, *Phys. Rev. B* 34 (1986) 4679–4684.
- [92] R.H. Wentorf Jr., J.S. Kasper, *Science* 139 (1963) 338–339.
- [93] Y.-X. Zhao, F. Buehler, J.R. Sites, I.L. Spain, *Solid State Commun.* 59 (1986) 679–682.
- [94] L. Rapp, B. Haberl, C.J. Pickard, J.E. Bradby, E.G. Gamaly, J.S. Williams, et al., *Nature Commun.* 6 (2015) 7555.
- [95] Z. Zhao, F. Tian, X. Dong, Q. Li, Q. Wang, H. Wang, et al., *J. Am. Chem. Soc.* 134 (2012) 12362–12365.
- [96] D. Ge, V. Domnich, Y. Gogotsi, *J. Appl. Phys.* 95 (2004) 2725–2731.
- [97] B. Haberl, M. Guthrie, S.V. Sinogeikin, G. Shen, J.S. Williams, J.E. Bradby, *High Pressure Res.* 35 (2015) 99–116.
- [98] A. Togo, F. Oba, I. Tanaka, *Phys. Rev. B* 78 (2008) 134106.
- [99] M.S. Hybertsen, S.G. Louie, *Phys. Rev. B* 34 (1986) 5390–5413.
- [100] L. Hedin, *J. Phys.: Condens. Matter* 11 (1999) R489–R528.
- [101] E.E. Salpeter, H.A. Bethe, *Phys. Rev.* 84 (1951) 1232–1242.
- [102] G.E. Jillison, M.F. Chisholm, S.M. Gorbatskin, *Appl. Phys. Lett.* 62 (1993) 3348–3350.
- [103] Reference Solar Spectral Irradiance: Air Mass 1.5 Homepage. <http://rredc.nrel.gov/solar/spectra/am1.5/>.